ORIGINAL ARTICLE



Impact of Deployable Solar Panels on Gravity Field Recovery in GRACE-like Satellites: a Closed-Loop Simulation Study

Andreas Leipner¹ • · Alexey Kupriyanov² • · Arthur Reis^{3,4} • · Annike Knabe² • · Manuel Schilling⁵ • · Vitali Müller^{3,4} • · Matthias Weigelt^{2,5} • · Jürgen Müller² • · Meike List⁵

Received: 17 December 2024 / Accepted: 7 June 2025 / Published online: 4 July 2025 © The Author(s) 2025

Abstract

Future satellite gravimetry missions must meet increasing scientific demands, requiring advanced technologies, e.g., novel inertial sensors, laser ranging systems and potentially electric thrusters to operate in a drag-free regime. Deployable solar panels offer a promising solution by providing sufficient power even under unfavorable illumination conditions, without significantly increasing satellite dimensions or mass. This study evaluates the impact of single and double deployable solar panels on gravity field recovery (GFR) through closed-loop simulations. Five GRACE-like satellite configurations were analyzed, each with distinct finite element models and inertia properties. Detailed orbit simulations included non-spherical static gravity field and impacting non-gravitational force models. Satellites drag coefficients varied from 2.25 to 4.5, depending on configuration. GFR was assessed using degree RMS of spherical harmonic coefficient differences between the recovered and reference fields. GFR results show that discrepancies between the modified and standard configurations are mainly driven by variations of the actuation noise of the modeled optical accelerometer - simplified gravitational reference sensor (SGRS). SGRS performance, in turn, depends on the satellite's cross-sectional area. Moreover, the convergence of residuals in the spectral domain for simulated orbits with different drag coefficients confirmed the dominant role of SGRS performance in the retrieved gravity field.

 $\textbf{Keywords} \ \ \text{Future satellite gravimetry missions} \cdot \text{Finite element modeling} \cdot \text{Satellite shapes} \cdot \text{Optical accelerometry} \cdot \text{Gravity field recovery} \cdot \text{Closed-loop simulation}$

> Alexey Kupriyanov kupriyanov@ife.uni-hannover.de

Arthur Reis arthur.reis@aei.mpg.de

Annike Knabe knabe@ife.uni-hannover.de

Manuel Schilling manuel.schilling@dlr.de

vitali Muller vitali.mueller@aei.mpg.de

Matthias Weigelt matthias.weigelt@dlr.de

Jürgen Müller mueller@ife.uni-hannover.de

Meike List meike.list@dlr.de

1 Introduction

Over the past two decades, satellite gravimetry missions have yielded distinctive datasets fundamental to a wide range of scientific and practical applications (Wiese et al. 2022). Three

- Institute for Satellite Geodesy and Inertial Sensing, German Aerospace Center (DLR), Am Fallturm 9, Bremen 28359, Germany
- Institute of Geodesy, Leibniz University Hannover, Schneiderberg 50, Hannover 30167, Lower Saxony, Germany
- Max Planck Institute for Gravitational Physics (IGP), Albert Einstein Institute, Callinstraße 38, Hannover 30167, Lower Saxony, Germany
- Institute for Gravitational Physics, Leibniz University Hannover, Callinstraße 38, Hannover 30167, Lower Saxony, Germany
- Institute for Satellite Geodesy and Inertial Sensing, German Aerospace Center (DLR), Callinstraße 30B, Hannover 30167, Lower Saxony, Germany



key missions, CHAMP (Torge et al. 2023), GOCE (Flechtner et al. 2021), and GRACE (Chen et al. 2022), alongside the currently operational GRACE-FO mission (Peidou et al. 2022), have contributed gravity field data products at varying spatial and temporal resolutions.

The data produced by these missions have been applied extensively in geophysical and environmental research. Examples include the analysis of glacier mass balance in Antarctica and Greenland (Otosaka et al. 2022), estimation of Glacial Isostatic Adjustment (Kang et al. 2022), terrestrial water storage assessments (Humphrey et al. 2023), and monitoring of gravitational variations originating from deep Earth processes (Chen et al. 2022). Furthermore, satellite gravimetry has proven useful in natural hazard assessments (e.g., floods and droughts) (Sun et al. 2017) and investigations into Earth's polar motion and length-of-day trends (Zotov et al. 2022).

Satellite gravimetry employs two primary measurement principles. The first approach, exemplified by GOCE, involves single-satellite gravity gradiometry, using onboard gradiometers to measure gravity gradients (Brockmann et al. 2014). The second approach, pioneered by the GRACE and GRACE-FO missions, involves the measurement of intersatellite distance variations in a low-low satellite-to-satellite tracking (Il-SST) configuration, using microwave ranging (Tapley et al. 2019). GRACE-FO further demonstrated the laser range interferometer (LRI) as a pathfinder instrument, anticipated to be a standard feature in future gravimetry missions (Müller et al. 2022).

Additionally, the concept of drag compensation, first implemented in GOCE, utilized an ion propulsion system to mitigate orbit decay and prevent accelerometer saturation, albeit with introduced thruster noise (Canuto 2018). This system probably will also feature in ESA's forthcoming next-generation gravimetry mission (NGGM), a paired-satellite mission in an inclined orbit designed for enhanced spatial-temporal resolution with five-day repeat cycles (Daras et al. 2023).

Despite these advancements, the spatial-temporal resolution offered by GRACE-like missions remains insufficient for numerous applications. Consequently, research has focused on augmenting mission accuracy, which can be categorized into two main approaches: enhancing inertial sensors, particularly accelerometers, and exploring alternative satellite formations.

The electrostatic accelerometers used in previous missions, such as GRACE(-FO) and GOCE, exhibit low-frequency drift that limits their precision (van Camp et al. 2021). However, the stringent requirements of the Laser Interferometer Space Antenna (LISA) gravitational wave detector have driven significant advancements in inertial sensing technologies, demonstrated with the LISA-Pathfinder mission (Armano et al. 2021). These advancements have

inspired a range of proposals for new electrostatic and optical accelerometers suitable for Earth observation (Dávila Álvarez et al. 2022; Weber et al. 2022). Additional studies have investigated the use of cold atom interferometers, both standalone and hybridized, for gravimetric sensing applications (Zahzam et al. 2022; HosseiniArani et al. 2024).

Further studies have evaluated the potential of multiple satellite pairs (Heller-Kaikov et al. 2023), novel tracking concepts such as high-low satellite-to-satellite tracking (Pail et al. 2019), configurations permitting cross-track measurements (Kupriyanov 2025), and small satellite constellations for monitoring sub-daily mass changes (Pfaffenzeller and Pail 2023).

Given the increased power demands anticipated for future ll-SST missions incorporating drag-compensated platforms and advanced inertial sensors (Dionisio et al. 2018), the use of larger solar arrays is under consideration. However, constraints on payload mass and volume within the launch vehicle fairing limit satellite size (Haagmans et al. 2020), motivating the development of deployable solar panel systems.

A key research question driving this study is whether the modified satellite shape, necessitated by the integration of novel inertial sensors, drag compensation system and nonoptimized solar illumination could compromise the quality of scientific data collected and reducing mission lifetime in future gravimetry missions. The need for highly accurate gravity field measurements is critical for advancing understanding of mass transport processes within the Earth system (Pail et al. 2015; Wiese et al. 2022). The altered satellite geometry may introduce asymmetries in mass distribution and surface area exposed to atmosphere, thereby increasing susceptibility to drag and thermal radiation effects. These perturbations could induce additional noise in the inter-satellite ranging measurements and degrade the performance of onboard accelerometers, potentially undermining the anticipated improvements from advanced inertial sensors.

This study evaluates modified satellite designs with respect to gravity field recovery (GFR). The paper is structured as follows: Chapter 2 discusses the challenges associated with future gravimetry missions, focusing on the implications of modified satellite shapes due to deployable solar panels. Chapter 3 provides an overview of the software used. Section 3.1 details the satellite dynamics simulation framework. In sect. 3.2, an accelerometer model featuring optical readout for test mass (TM) displacement is presented. Section 3.3 explains the functional and stochastic modeling in GFR simulations. Major error sources and assumptions that took place in the simulation procedure are listed in the sect. 3.4. Chapter 4 discusses the orbit simulation and GFR results. The paper ends with Chapter 5 where discussion of the results is presented.



59

2 Challenges of future gravimetry missions and modeling of the modified satellite shapes

Proposals for next-generation gravimetry missions include the deployment of satellite pairs in constellation configurations, similar to current ll-SST missions (Haagmans et al. 2020). However, several mission parameters are anticipated to differ in these successor missions. To enhance gravity signal resolution, future missions may operate at lower orbital altitudes, which will amplify the gravity signal but also increase the influence of atmosphere disturbance forces. Mission lifetimes are projected to span at least one full 11-year solar cycle to ensure comprehensive temporal coverage (Dionisio et al. 2018), during which the satellites will experience the full variation in solar radiation pressure (SRP) effects.

An ion thruster system is planned to enable enhanced attitude and orbit control, including precise drag compensation (Haagmans et al. 2020). This system is estimated to require approximately 1 kW of power (Dionisio et al. 2018); however, this demand could increase with the inclusion of advanced electrostatic accelerometers or inertial sensors equipped with optical test mass (TM) readouts on future missions. Additionally, the non-sun-synchronous orbits proposed for these missions will result in varying solar illumination conditions, impacting the solar panels' power generation. This variability necessitates careful consideration in detailed pre-mission analysis to ensure adequate power supply.

For reference, the currently operating GRACE-FO mission, equipped with gallium arsenide solar arrays, achieves a power production of approximately 1.37 kW (Kornfeld et al. 2019). However, this may prove insufficient for future missions, given the anticipated higher power demands.

The mission design requires that both satellites be launched and deployed in orbit simultaneously to establish the necessary paired configuration. Critical constraints include the geometrical limitations of the launch vehicle fairing and the total allowable payload mass, which future gravimetry missions must accommodate to ensure mission viability (Dionisio et al. 2018; Haagmans et al. 2020).

To address the anticipated power demands of future gravimetry satellites, deployable solar panels present a feasible solution. These panels can remain folded during launch, minimizing the satellite's surface dimensions within the fairing constraints. Once deployed, however, the expanded surface area will increase susceptibility to atmospheric drag and SRP. As a result, the effects of this increased drag and SRP must be carefully modeled and accounted for in the gravity field recovery process to maintain data accuracy.

To evaluate the implications of these expanded surface areas, this study employed Finite Element (FE) model-

ing to simulate different satellite shapes inside Extended High Performance Satellite Dynamics Simulator (XHPS). By comparing shapes with deployable panels in varied positions, such as top-mounted and bottom-mounted orientations, the simulated models allowed for detailed analysis of how these designs impact GFR.

The FE models of satellite configurations evaluated in this study are presented in Fig. 1. For comparison, the standard GRACE-FO satellite body, represented by a trapezoidal prism, is shown in Fig. 1a, with dimensions and mass consistent with the actual GRACE-FO satellite (1.942 m × $3.123 \,\mathrm{m} \times 0.72 \,\mathrm{m}$, 601.214 kg (NASA 2002)). The surface properties (reflectivity, absorption and emission (NASA 2002)) are assigned to the corresponding finite elements to maintain consistency with the actual satellite configuration. Additionally, four modified satellite designs incorporating deployable single or double solar panels, mounted either on the top (Fig. 1b/1d) or bottom (Fig. 1c/1e) of the satellite body, are evaluated. These configurations could potentially increase power generation by approximately 1 kW for the single solar panel or 2 kW for the double solar panels, meeting the enhanced energy requirements for future mission instruments and control systems.

An additional consideration is the potential obstruction of the star tracker cameras' field-of-view due to various solar panel configurations. While this effect was not addressed in this study, it remains essential to account for these implications in future mission design.

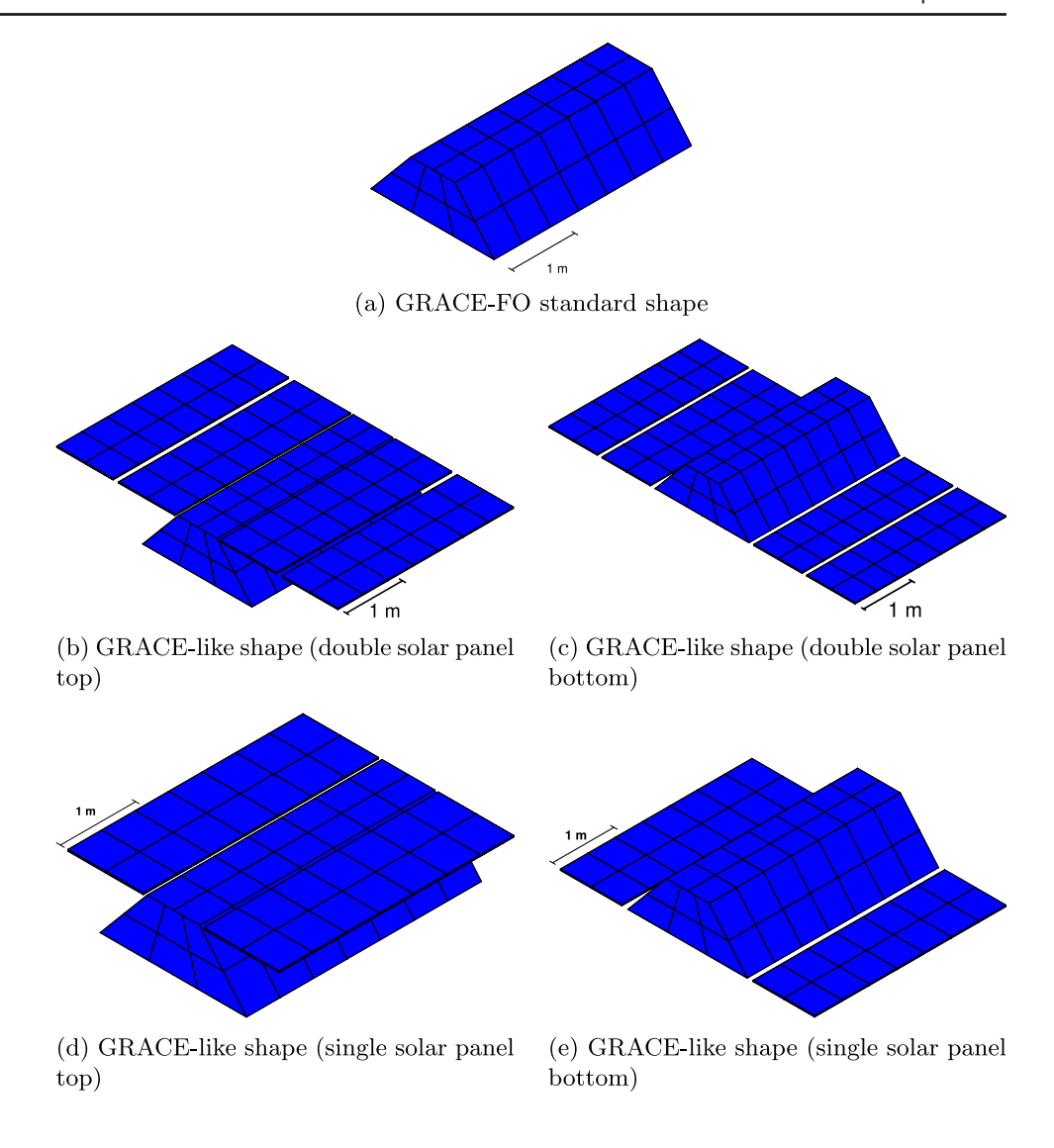
3 Overview of the closed-loop simulation procedure and software parts

The simulation methodology applied in this study is depicted in Fig. 2. It consists of multiple interconnected modules, each representing a distinct software tool that can function independently or, as in this instance, as part of an integrated simulation and data analysis workflow. The combination of the Extended High Performance Satellite Dynamics Simulator (XHPS) and Accelerometer Modeling Environment (ACME) modules facilitates the generation of scientific datasets for a prospective Il-SST mission, while the Quantum Accelerometry (QACC) software module is employed to derive the corresponding gravity field solutions.

Orbital disturbance forces are strongly influenced by the satellite's complex geometry, even when assuming a homogeneous distribution of optical properties across its external surfaces (List et al. 2015). To accurately capture the effects of these disturbance forces for the FE models from Fig. 1, corresponding lookup tables were generated through a preprocessing algorithm to facilitate subsequent use in the satellite dynamics simulator.



Fig. 1 FE models of the studied satellite shapes



The orbital dynamics were simulated using the XHPS software developed by ZARM/DLR (Wöske et al. 2016). XHPS enables precise definition of key mission parameters, including the initial position and velocity of the satellite(s), as well as their orientation. The software incorporates a FE model of the satellite(s) to allow detailed modeling of disturbance forces based on satellite geometry. Additionally, the simulation incorporates non-gravitational forces along with a provided reference gravity field model into the orbit integrator.

The multi-degree-of-freedom accelerometer was modeled at the Max Planck Institute for Gravitational Physics (IGP) using a Matlab/Simulink-based tool named Accelerometer Modeling Environment (ACME) (Kupriyanov et al. 2024b). The model parameters adhered to the specifications outlined in the proposed simplified gravitational reference sensor (SGRS) framework (Dávila Álvarez et al. 2022). Operating concurrently with XHPS, ACME generated the accelerome-

ter noise budget, represented as amplitude spectral densities in the frequency domain.

GFR simulations were executed on the Leibniz University IT Services (LUIS) cluster (LUIS 2024) using the QACC toolbox, developed at the Institute of Geodesy (IfE) (Wu 2016). In this setup, synthetic noisy observations are generated based on satellite positions from XHPS, incorporating various modeled error sources. Specifically, the stochastic component encompasses all error contributors, including inter-satellite range instrument noise time series, and sourced from ACME, SGRS noise time series. Subsequently, gravity field recovery is performed, and the retrieved gravity model is compared to the reference model (EIGEN-6C4), with results evaluated based on the residuals. The following sections provide detailed descriptions of each module within the simulation procedure.



Fig. 2 Block diagram of the closed-loop simulation procedure. * simplifications of orbit dynamics has been considered. ASD - Amplitude Spectral Density; QACC - Quantum Accelerometry (gravity field recovery tool for Il-SST)

3.1 Satellite dynamics simulator

The satellite dynamics simulator's (XHPS) primary purpose is to generate data that can be used in the GFR process. It is designed to accurately model the satellite's behavior by taking into account various disturbance forces such as non-spherical gravitational fields, atmospheric drag and SRP. Additionally, the simulator incorporates the geometry of the satellite(s) into its calculations on the basis of FE models. In that way, it provides a detailed and realistic dataset that helps understand the impact of satellite shapes on GFR, ultimately aiding in the refinement of satellite geodesy techniques and improving the precision of geophysical measurements.

Earth's gravitational field

The modeling of gravitational fields in the simulator is based on spherically harmonics, which provide a mathematical framework for representing the Earth's gravitational field (Wertz 1980):

$$V(r,\phi,\lambda) = \frac{\mu}{r} \sum_{l=0}^{l=90} \left(\frac{a_e}{r}\right)^l \sum_{m=0}^l P_{l,m} \left(\sin\phi\right) \cdot \left[C_{l,m} \cos m\lambda + S_{l,m} \sin m\lambda\right], \tag{1}$$

where μ is the product of the universal constant of gravitation G and the mass of the Earth M, a_e is the semi-major axis of the Earth's reference ellipsoid, r, ϕ , λ are the satellite distance, latitude and longitude, respectively in a body-fixed coordinate system, $C_{l,m}$ and $S_{l,m}$ are the fully normalized spherical harmonic coefficients of degree l and order m and $P_{l,m}$ are the fully normalized associated Legendre Functions of degree l and order m. Each term in the series corresponds to a different frequency component, capturing variations in the gravitational potential, including irregularities such as the equatorial bulge and local anomalies (for computations l and m are set to values from table 1). This allows for a description of the field and determination of the gravitational acceleration on the satellite.

Atmospheric drag

Atmospheric drag is known to be one of the most disturbing effects at the appropriate orbit height for gravimetry missions (Rievers et al. 2019). The simulator is accounting for variations in the Earth's atmosphere at mission's orbit height, as well as the disturbance acceleration due to the geometry of the satellite. The force is calculated via the FE model approach.



The atmospheric drag force $d\vec{f}_{\text{drag}}$ acting on one of the FE model elements with the outward normal vector \vec{n} and surface area dA can be calculated by (Wertz 1980)

$$d\vec{f}_{\text{drag}} = -\frac{1}{2}c_D\rho v^2(\vec{n}\cdot\vec{v})\vec{v}dA, \qquad (2)$$

where \vec{v} is the unit vector in the direction of the satellites velocity relative to the atmosphere around it, ρ is the atmospheric density, c_D is the drag coefficient and v is the norm of the relative velocity vector. The total atmospheric drag force can be calculated by summing up all forces acting on each FE model element. The atmospheric density is calculated during the simulation at each time step and current satellite location. This ensures a high resolution in time and space of the drag disturbance force.

Solar radiation pressure

Precise orbital calculations and long-term mission planning, particularly for satellites with large surface areas, must account for the forces exerted on the satellite by solar radiation. The simulator accounts for solar disturbance acceleration by calculating it using the FE model approach and assuming parallel Sun rays striking the satellite.

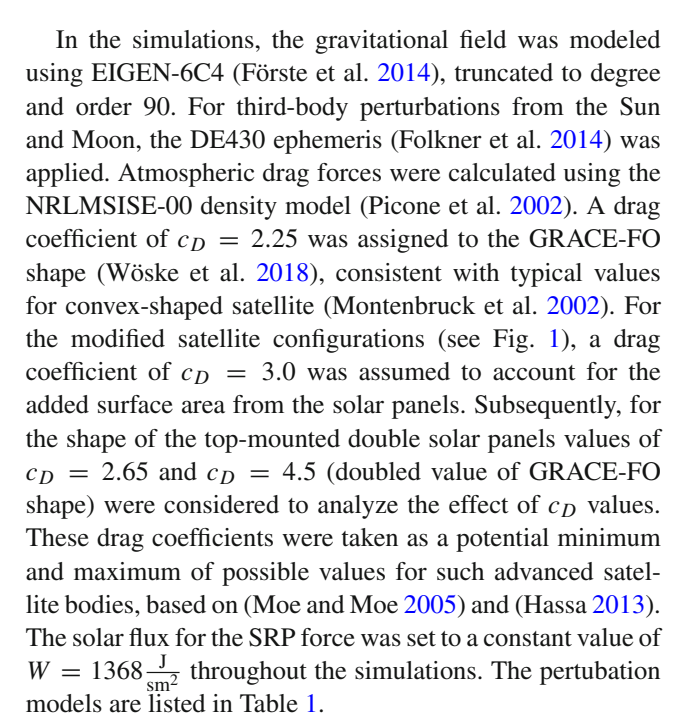
The SRP force df_{SRP} acting on one of the FE model elements with the outward normal vector \vec{n} and surface area dA can be calculated as (Wertz 1980)

$$d\vec{f}_{\text{SRP}} = -P \left[(1 - c_s) \vec{s} + 2 \left(c_s \cos \theta + \frac{1}{3} c_d \right) \vec{n} \right] \cos \theta dA, \tag{3}$$

where P is the solar flux at the satellites position, \vec{s} is the unit vector from the satellite to the sun and θ is the angle between the FE model element normal vector \vec{n} and the vector \vec{s} . The coefficients c_s and c_d are for specular and diffuse reflection. Like for the atmospheric drag force, the total SRP force can be calculated by summing over all forces acting on each FE model element. Earth's shadow is implemented entirely geometric, so a disk is shadowing the satellite.

These forces are highly dependent on the satellites' shape, as the effective area, force coefficients, and force directions are influenced by the satellites' geometry. For more detailed explanation on the selected satellite shapes see sect. 2.

The simulator implements the equations for drag and solar radiation pressure (SRP) within a preprocessing algorithm that generates lookup tables to manage the complex computations required for precise force determination. Initially, this algorithm calculates the drag force and SRP force for a specified range of incidence angles. The precomputed values are then stored in lookup tables, which the simulator references during runtime to efficiently and accurately determine disturbance forces at each time step.



The initial conditions for all satellite pairs and simulations are listed in Table 2. These initial parameters, including the start date of January 1, 2008, and an attitude control system mode of "line of sight (LoS) Pointing" via a PID controller, were kept constant for all simulations to isolate the effects of the satellite shapes. The values of position and velocity are provided by the GROOPS software (Mayer-Gürr et al. 2021), developed by the Institute of Geodesy at Graz University of Technology, based on the GRACE orbits.

The satellite's mass is set to 601.214 kg, with its inertia tensor defined as specified in Table 3 (Wen et al. 2019). For the modified configurations featuring single solar panels, an additional mass of 7.8 kg is included, calculated based on the density of 1.25 $\frac{kg}{m^2}$ for the triple-junction Galliumarsenid (GaAs) GRACE-FÖ solar panels (Satsearch 2024). For configurations with double solar panels, an additional mass of 15.6 kg is accounted for. The inertia tensor for the modified satellite shapes is computed using the Parallel Axis Theorem, applied to the GRACE-like shape to account for added mass and altered mass distribution. Due to the symmetric placement of the additional solar panels in the lateral directions relative to the satellite center of mass, and the small mass contribution (1.3%-2.6%) of the total mass), the changes to the off-diagonal terms of the inertia tensor were found to be negligible compared to satellite body's intrinsic products of inertia. Therefore, for all configurations, the off-diagonal elements were assumed unchanged, while the principal moments of inertia and the mass were updated accordingly. The resulting values are listed in Table 3.



Pertubation	Model	Remark	
Static gravity field	EIGEN-6C4 [1]	Considered till d/o 90	
Ephimeris model	DE430 [2]	-	
Third bodies	_	-	
- Sun			
- Moon			
Non-gravitational Forces	-	-	
Air drag	Density model: NRLMSISE-00 [3]	- Effective area reevaluated each time step	
Solar radiation pressure	SRP calculation: parallel sun rays Constant solar flux: $W = 1368 \frac{J}{\text{sm}^2}$	 Eclipse calculation: geometric cylindrical eclipse Ilumination condition reevaluated each time step 	

Table 2 Initial conditions for all satellites with initial date, position, velocity and attitude control system (ACS). Position and velocity of the satellites are provided by GROOPS (Mayer-Gürr et al. 2021)

Satellite	Position [m]	Velocity [$\frac{m}{s}$]	Date	ACS
Satellite A	x: 1.04106912 · 10 ⁶	x: 1.68961 · 10 ³	2008-01-08	LoS
	y: $3.37233841 \cdot 10^6$	y: $6.30209 \cdot 10^3$	00:00:00	
	$z: -5.87039994 \cdot 10^6$	z: $3.93698 \cdot 10^3$		
Satellite B	x: $1.09381033 \cdot 10^6$	$x: 1.64626 \cdot 10^3$	2008-01-08	LoS
	y: $3.57174758 \cdot 10^6$	y: $6.16464 \cdot 10^3$	00:00:00	
	z: $-5.74121787 \cdot 10^6$	z: $4.16732 \cdot 10^3$		

Table 3 Satellite properties for simulation

Satellite	Mass [kg]	Inertia Tensor [kgm ²]
GRACE-FO	601.214	$\begin{pmatrix} 110.49 & -1.02 & 0.35 \\ -1.02 & 580.67 & 0.04 \\ 0.35 & 0.04 & 649.69 \end{pmatrix}$
GRACE-like Single Solar Panel Top	609.014	$\begin{pmatrix} 120.76 & -1.02 & 0.35 \\ -1.02 & 588.50 & 0.04 \\ 0.35 & 0.04 & 664.81 \end{pmatrix}$
GRACE-like Single Solar Panel Bottom	609.014	$\begin{pmatrix} 132.79 & -1.02 & 0.35 \\ -1.02 & 587.56 & 0.04 \\ 0.35 & 0.04 & 677.78 \end{pmatrix}$
GRACE-like Double Solar Panels Top	616.814	$\begin{pmatrix} 155.92 & -1.02 & 0.35 \\ -1.02 & 596.33 & 0.04 \\ 0.35 & 0.04 & 704.84 \end{pmatrix}$
GRACE-like Double Solar Panels Bottom	616.814	$\begin{pmatrix} 191.53 & -1.02 & 0.35 \\ -1.02 & 594.46 & 0.04 \\ 0.35 & 0.04 & 742.32 \end{pmatrix}$

3.2 Simplified GRS optical accelerometer modeling in ACME

This study employs an optical accelerometer, referred to as the simplified gravitational reference sensor (SGRS), as the inertial sensor. In the context of future satellite gravimetry missions, the impact of modified satellite shapes on gravity field recovery is, in principle, independent of the specific type of accelerometer used. However, optical inertial sensors offer several advantages over electrostatic, cold atom interferometry (CAI)-based, or hybrid instruments. Optical accelerometers, also known as gravitational reference sensors (GRS), were successfully operated during the LISA Pathfinder mission. As a result, they benefit from a higher technology readiness level due to their proven flight heritage compared to CAI instruments. Furthermore, they offer significant performance enhancements over state-of-the-art electrostatic accelerometers, such as SuperSTAR. These improvements include advanced test mass displacement readout techniques utilizing optical interferometry, a



cubic test mass design enabling highly sensitive multi-axis measurements, and a wireless charge management system, among other innovations (Kupriyanov et al. 2024b, a). These features make optical accelerometers a compelling choice for improving gravity field recovery.

The SGRS model used in this study is primarily based on the parameters proposed in (Dávila Álvarez et al. 2022), incorporating a laser interferometer for test mass displacement readout. It is implemented within the ACME simulation environment. However, compared to the SGRS described in (Dávila Álvarez et al. 2022), the thermal stability in the low-frequency domain is still under evaluation. Its impact is assumed to be more pronounced than reported in (Dávila Álvarez et al. 2022), with thermal noise characteristics similar to those observed in the MicroSTAR electrostatic accelerometer (Christophe et al. 2018; Dalin et al. 2020).

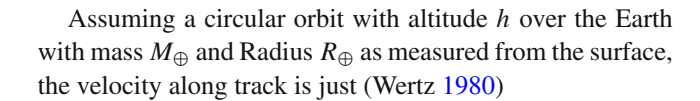
Additionally, for actuation noise-related to the stability of the reference voltage applied to the actuation electrodes-a reference voltage of 10 V with a stability of 0.6 ppm/ $\sqrt{\text{Hz}}$ was assumed, following the specifications in (Mance 2012; Halloin et al. 2013). All other accelerometer noise sources were adopted as detailed in (Kupriyanov et al. 2024b). The simulations considered a freely levitating cubic gold-platinum test mass with 40 mm sides and a 1 mm gap between the test mass and the surrounding electrode housing.

Given that this study examines various satellite shapes, the actuation noise level of the inertial sensor deserves more detailed attention. Non-gravitational forces influence the TM through the coupling between the satellite and the TM (Josselin et al. 1999). Consequently, the actuation noise level is expected to vary depending on the cross-sectional area of the satellite, as this directly affects the magnitude of the coupling forces.

Simplifications were introduced in the modeling of non-gravitational forces to estimate the actuation noise of the SGRS (denoted with an asterisk in Fig. 2). Specifically, the system was treated as a single degree of freedom in the along-track direction, with atmospheric drag considered the dominant non-gravitational perturbation and the sole non-conservative force accounted for in ACME. Under these assumptions, the resultant acceleration of a satellite with mass M in the along-track direction is dependent on the local atmospheric density ρ , the satellite velocity v, the cross-sectional area A_{SC} , and the drag coefficient c_D .

$$a_{\text{non-grav}} = \frac{1}{2} \frac{\rho v^2 c_D A_{SC}}{M},\tag{4}$$

which is a simplified version of eq. 2. The density can be determined without running the complex models that are built-in XHPS by using a simpler atmospheric model such as Harris-Priester, where the density is a function of altitude $\rho = \rho(h)$ (Cappellari 1976).



$$v = \sqrt{\frac{GM_{\oplus}}{(R_{\oplus} + h)}}. (5)$$

The coulombic force that levitates a TM of mass m, that forms a capacitor with an electrode of area A_{el} and gap d, which is maintained in a potential difference V is (Josselin et al. 1999)

$$F = ma_{\text{actuation}} = \frac{1}{2} \frac{\epsilon_0 A_{el}}{d^2} V^2. \tag{6}$$

Where ϵ_0 is the dielectric constant of vacuum. Since the actuation of the electrode keeps the TM centered in its housing, the non-gravitational accelerations perceived by the satellite are thus coupled to the TM:

$$|a_{\text{non-grav}}| = |a_{\text{actuation}}|$$
 (7)

inserting these equations into eq. 6 we have the value of voltage required to constantly re-center the TM:

$$V = \sqrt{\frac{d^2}{\epsilon_0 A_{el}} \frac{m}{M} c_D A_{SC} \rho(h) \left(\frac{GM_{\oplus}}{R_{\oplus} + h}\right)}.$$
 (8)

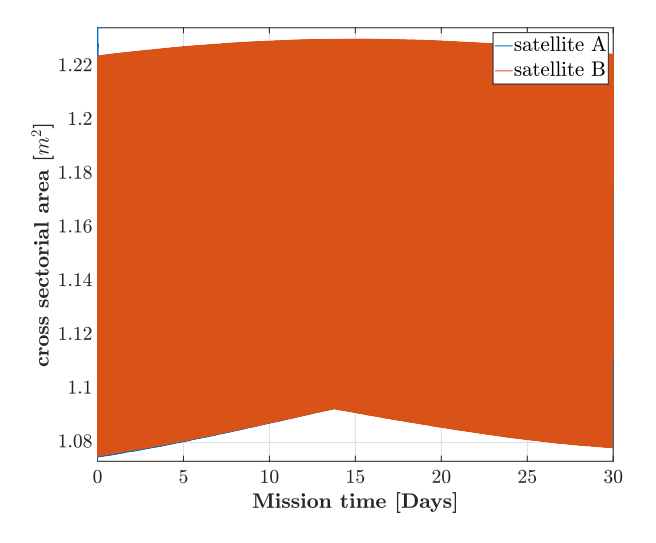
Therefore, even in a back-of-the-envelope scenario, where everything is ideal but the voltage reference stability, we expect an associated actuation noise dependent not only on the accelerometer design but also on the satellite and orbit characteristics.

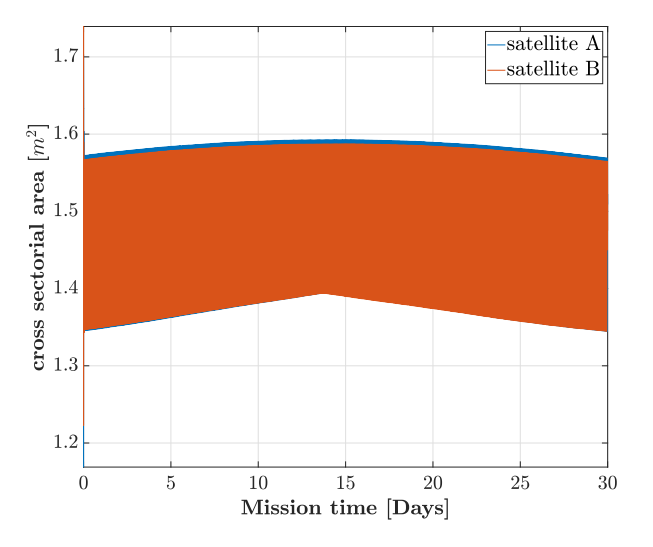
From the orbital simulations carried out in XHPS, a value for the monthly averaged cross-sectorial area of $1.16\,\mathrm{m}^2$ was derived for the GRACE-FO standard shape, $1.32\,\mathrm{m}^2$ for the GRACE-like case with a single panel and $1.47\,\mathrm{m}^2$ for the GRACE-like case with double solar array (see Fig. 3).

Figure 4 shows the amplitude spectral densities (ASD) of the modeled inertial sensors and inter-satellite LRI that were used in the gravity field recovery simulations. The total noise budget in terms of ASD of the modeled SGRS for the 'standard' (black curve), GRACE-like with single panel (red curve) and GRACE-like with double solar array (blue curve) is shown. The difference between the curves above 1 mHz is due to the different level of the actuation noise. Also, an amplitude spectral density of the measurement error of the inter-satellite laser range interferometer (Kupriyanov et al. 2024b) (gray dotted line) anticipated in 2033 is shown. It is clear that the errors of the inter-satellite LRI dominate over the SGRS noise in the high-frequency domain.

The colored noise of the modeled SGRS in the lowfrequency domain is mainly caused by thermal instability







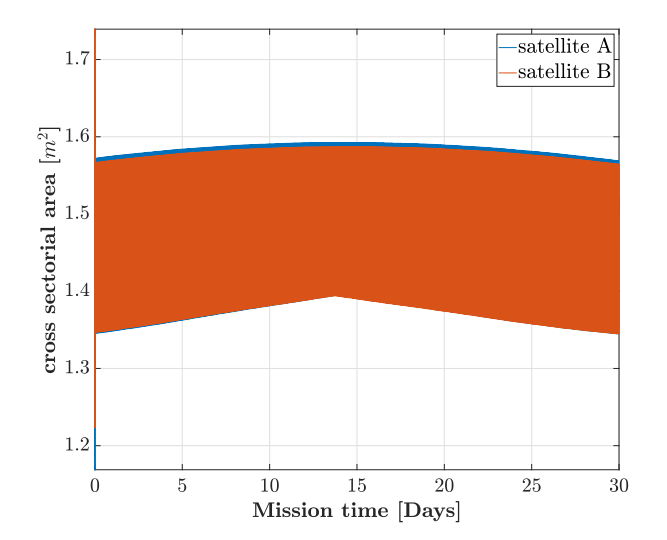


Fig. 3 Cross-sectorial areas of the investigated satellite shapes during simulation

noise. Therefore, the generated noise time series includes a low-frequency component ($\sim 10^{-10}\,\mathrm{m/s^2\sqrt{Hz}}$ at $10^{-4}\,\mathrm{Hz}$) that causes the drift. These noise time series were used in the generation of the synthesized noisy observations of the GFR (see Fig. 2).

3.3 Functional model, stochastic modeling and assumptions in GFR simulation

GFR simulations were conducted to assess the performance differences between the GRACE-FO satellite shape and its modified counterparts. Following the framework outlined in Fig. 2, synthetic noisy observations were generated for various decaying orbits, incorporating multiple error sources. The simulations considered three accuracy levels of the modeled SGRS optical accelerometer, accounting for the effects

of different satellite shapes, as shown in Fig. 4, as part of the stochastic error component. Additionally, errors arising from the inter-satellite laser ranging instrument were included in the analysis.

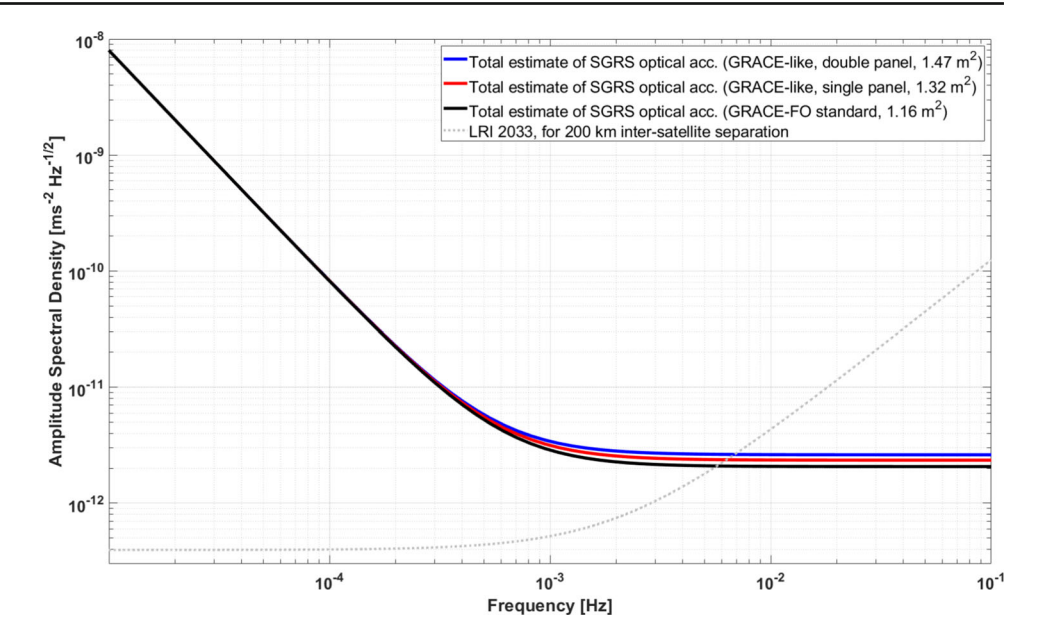
The approximate acceleration-based solution approach (Weigelt 2017) is implemented in the QACC software. In this method, observations are first collected along the orbit at specific measurement positions and subsequently linked to the gradient of the gravitational potential (∇V). The functional model for ll-SST observations implemented in the QACC toolbox is expressed as follows:

$$\ddot{\rho} = \nabla V_{AB} \cdot \vec{e}_{AB}^a + \dot{\vec{x}}_{AB} \cdot \dot{\vec{e}}_{AB}^a. \tag{9}$$

Here, $\ddot{\rho}$ represents the range acceleration, ∇V_{AB} denotes the gradient of the gravitational potential, and \dot{e}_{AB}^a is the time



Fig. 4 Amplitude spectral density of the total noise budget of the modeled SGRS optical accelerometers for the 'standard' GRACE-FO shape (black curve) and modified ones (blue and red curves) and the anticipated measurement error of the inter-satellite LRI in 2033 for the satellites separated by 200 km (gray dotted line)



derivative of the unit vector along the LoS between the two satellites. In the QACC software, the second term of equation (9) is neglected (Knabe 2023). This omission of the so-called centrifugal term removes the orbit-dependent contribution, masks the influence of satellite shapes, and results in an optimistic scenario. The system of linear equations is then solved using least-squares adjustment to determine the spherical harmonic coefficients of the gravity field. According to (Niemeier 2008) the estimated solution \hat{x} that minimizes the sum of squares of the weighted residuals in LS adjustment, is given by:

$$\hat{\vec{x}} = \left(\mathbf{A}^T \mathbf{P} \mathbf{A}\right)^{-1} \mathbf{A}^T \mathbf{P} \vec{l} = \mathbf{N}^{-1} \vec{w},\tag{10}$$

where **A** the design matrix, $\mathbf{P} = \mathbf{\Sigma}_{ll}^{-1}$ the weight matrix (obtained from stochastic modeling), \vec{l} the observation vector, **N** the normal matrix and $\vec{w} = \mathbf{A}^T \mathbf{P} \vec{l}$.

An empirical stochastic modeling approach, involving iterative optimization of the weights, was employed in the gravity field recovery routine for multiple purposes, for example: to down-weight and de-correlate the synthesized colored noise observations (Knabe 2023), thereby enhancing the signal-to-noise ratio (Luthcke et al. 2013) and improving the estimation of the spherical harmonic coefficients, etc. Initially, the normal matrix \mathbf{N} is constructed using a unit weight matrix \mathbf{P} , which corresponds to white noise. Afterward, the full variance-covariance matrix of the measurements $\mathbf{\Sigma}_{II}$, is constructed from a biased estimation of the auto-covariance vector \vec{r} and iteratively computed from the post-fit residuals \hat{v}_n . According to (Koch et al. 2010), the auto-covariance

element r_i is estimated as

$$r_i = \frac{1}{N} \sum_{n=0}^{N-1-|i|} \hat{v}_n \cdot \hat{v}_{n+i}, \tag{11}$$

where N is the length of the observations, i.e., 1 month and i = [0; N-1]. The absolute value |i| ensures that the summation indices remain within valid bounds of the residual sequence for all lags. Moreover, as noted in Koch et al. (2010), the use of the biased estimator is justified since the unbiased alternative results in large variances for lags i approaching N. Finally, assembled variance-covariance matrix of the observations Σ_{ll} is decomposed by the Cholesky approach.

Empirical stochastic modeling influences the residuals by incorporating all considered noise sources, including intersatellite LRI measurement errors, SGRS noise components, and least-squares adjustment errors. The GFR results presented in this study were obtained after three iterations of weight optimization, as the solutions showed convergence at this point. The posterior variance $\hat{\sigma}_0^2$ of the post-fit residuals quantifies the solution's quality (Wu 2016):

$$\hat{\sigma}_0^2 = \frac{\vec{\hat{v}}^T \mathbf{P} \hat{v}}{s - r} = \frac{\vec{l}^T \mathbf{P} \vec{l} - \vec{w}^T \hat{x}}{s - r},\tag{12}$$

where s the number of observations and r the number of parameters.

As outlined in sect. 3, the evaluation of results is performed at the level of the residuals by comparing the recovered gravity field model with the reference gravity field. To quantify the differences, unitless spherical harmonic coefficient discrepancies, referred to as true errors, between the reference and



recovered gravity field models are multiplied by the Earth's radius, yielding geoid height deviations in meters.

Time-variable background models and the associated aliasing errors represent significant limitations in current satellite gravimetry (Purkhauser and Pail 2020). However, these factors were not considered in this study, as the primary focus is on comparing the performance of the 'standard' GRACE-FO satellite shape with the modified configurations, which incorporate the novel SGRS optical accelerometer. This advanced inertial sensor, along with the anticipated low error levels of the inter-satellite laser range interferometer, has noise characteristics well below the order of magnitude of time-variable background model errors.

Aliasing effects, which stem from instrument noise and inaccuracies in background models, can significantly impact the accuracy of satellite gravimetry solutions. Improving both of these factors is crucial for achieving more precise results. Time-variable background models are continuously being refined, as demonstrated by advancements such as the release of the Atmosphere and Ocean De-Aliasing Level-1B product RL07 (Shihora et al. 2022) and the recently available AOe07 (Shihora et al. 2024). Furthermore, the upcoming Mass-change And Geosciences International Constellation (MAGIC) mission, which consists of two satellite pairs, is expected to greatly expand the range of observable mass-change phenomena and resolve significantly smaller spatial scales compared to a near-polar standalone satellite pair (Daras et al. 2023).

3.4 Error analysis

Various error sources and underlying assumptions influence the accuracy of the results throughout each simulation phase, including orbital dynamics, SGRS modeling, and gravity field recovery. These factors can introduce deviations that need to be carefully considered. Table 4 provides a summary of the major error sources identified in the simulation procedure. The listed error sources include systematic, random and numerical errors arising from modeling assumptions, measurement noise, and finite precision computations. Gross errors, defined as large and infrequent deviations typically caused by sensor faults or unexpected anomalies, were not considered in this study.

It is important to note that the various error sources listed in Table 4 differ fundamentally in nature, and a direct, uniform quantification of their magnitude is not feasible. However, based on physical modeling insights and experience from similar GFR simulations, three dominant error sources can be identified (one from each utilized software tool). In XHPS, integration errors are considered the most influential, as the cumulative effect of small inaccuracies during numerical integration can significantly impact the simulated orbit. Moreover, with non-optimal initial conditions,

the inter-satellite distance and orbital altitude could deviate by several kilometers compared to the optimized case, which in turn would significantly affect the output results. In ACME, measurement errors are identified as the dominant source, since various sensor imperfections are combined under this category, and modifying any of these components can directly influence the accuracy of the retrieved gravity models. Finally, in QACC, approximation errors are considered the most critical, as numerous assumptions and simplifications are introduced during the GFR process.

4 Results

4.1 Satellite orbit simulation and force calculation results

Figure 5a illustrates the variation in SRP force magnitude as a function of the incident solar rays direction on the satellite geometry calculated by the preprocessing algorithm for the GRACE-FO shape shown in Fig. 1a. Figure 5b shows the polar angle $(0-\pi)$ and azimuth angle $(0-2\pi)$ defining the direction of the incoming sun rays relative to the satellite's reference frame during preprocessing. The color scale encodes the magnitude of the force generated by the incident solar rays. Higher values on the color scale correspond to greater force magnitudes, suggesting stronger interactions between the solar radiation and the satellite surface. This plot effectively captures the anisotropic nature of the force distribution, highlighting how the satellite geometry responds differently to solar radiation depending on the direction of incidence.

Figure 6 depicts the variation in differences in force magnitude between each analyzed satellite shape and the GRACE-FO shape. The results indicate that the double solar panel bottom shape exhibits the highest forces, while the single solar panel top shape produces a force profile most similar to that of the GRACE-FO shape. The presence of additional solar panels, as well as the gaps between these panels and the main satellite body, introduces distinct arched like structures in the force profiles, which is due to solar panel gaps allowing light to pass through to the geometry below at certain angles of incidence.

The orbital simulations were conducted under a non-drag-compensated regime, with a drag coefficient of $c_D=2.25$ assigned to the GRACE-FO configuration, and $c_D=2.65$, 3.0 and 4.5 for the modified satellite shapes. The orbital decay of the GRACE-FO satellite over a one-month period is shown in Fig. 7a, represented by the maximum orbital altitude recorded for each orbit. Figure 7b illustrates the differences in orbital decay between each modified satellite shape (with $c_D=3.0$) and the GRACE-FO configuration. The results show that satellite shapes with increased reference areas,



59 Page 12 of 19 A. Leipner et al.

Table 4 List of major error sources in the simulation procedure

Software	Type of error	Description
Orbital dynamics (XHPS)	Integration Errors	Accumulation of small errors during numerical integration due to finite step size, leading to divergence
	Numerical Errors	Truncation errors and round-off errors arise from finite precision of floating-point arithmetic and the omission of higher-order terms
	Modeling Errors	Mathematical description of disturbance forces use simplified assumptions
SGRS modeling (ACME)	Numerical Errors	Errors from the LPSD (Logarithmic frequency axis Power Spectral Density) algorithm in obtaining the PSD of the instruments from the time domain signals
	Modeling Errors	Assumptions in reference voltage stability may be too optimistic
	Processing Errors	Noise budget estimation in the frequency domain using transfer func- tions may introduce numerical inaccuracies
	Measurement Errors	Sensor imperfections, e.g., thermal noise, capacitive sensing noise, and actuation noise in the SGRS model
	Instrumental Errors	Electrostatic and optical sensor limitations, such as laser interferometric readout accuracy or voltage fluctuations
	Alias Errors	Potential spectral leakage and aliasing due to discrete sampling and windowing effects in the spectral analysis
GFR (QACC)	Approximation Errors	The omission of the centrifugal term in the functional model eliminates certain effects and leads to an optimistic scenario
		The gradient of the gravitational potential was calculated between the positions of two satellites, assuming perfect orbit determination without any attitude errors
		No scale factor of ACCs or calibration was considered
		Time-variable background models and associated errors were not included in GFR
	Numerical Errors	Finite precision of floating-point arithmetic in Fortran
	Least-Squares Adjustment Errors	The inversion of the normal matrix may lead to an amplification of noise
	Stochastic Modeling Errors	Improper noise assumptions, may lead to non-optimal weighting of observations and biased error propagation
	Truncation Errors	GFR solutions were truncated and computed only up to degree and order 90
	Validation Errors	Relevant features of the output signal may be not fully captured within EWH or degree RMS representation, potentially leading to the omission or masking of certain characteristics

and consequently higher drag forces, experience faster orbital decay compared to the GRACE-FO case.

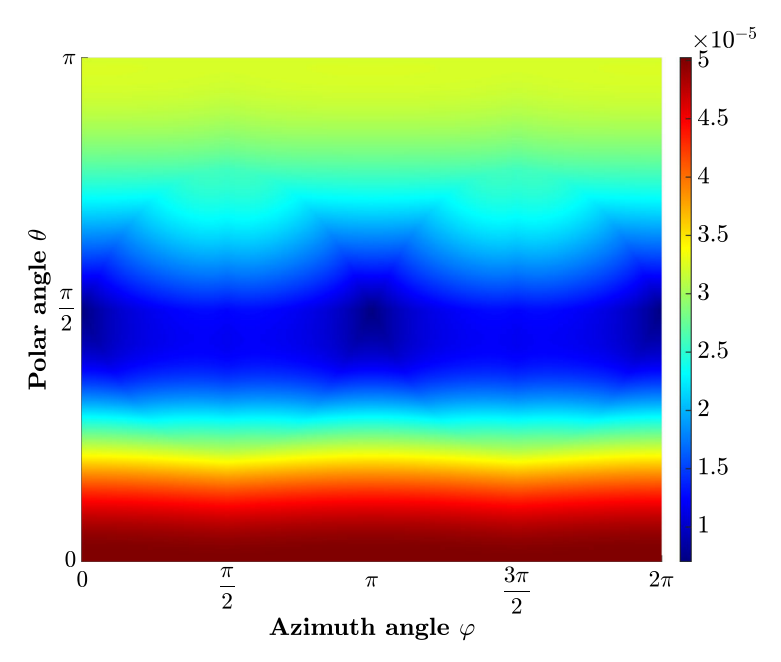
Figure 8 illustrates the maximum and minimum values of the inter-satellite distance, defined as the separation between the two satellites during the simulation. The figure also includes the maximum and minimum values of the inter-satellite distance derived from the reduced dynamic orbit data provided by the Technical the University of Graz (Mayer-Gürr et al. 2021). Initially, the simulated inter-satellite distance aligns closely with the Graz-derived values. However, as the simulation progresses, slight deviations emerge. These discrepancies can be attributed to unmodeled disturbances, modeling inaccuracies, and numerical errors (see table 4).

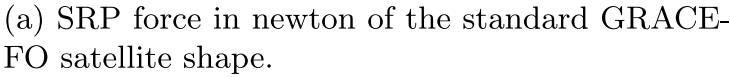
4.2 GFR simulation results

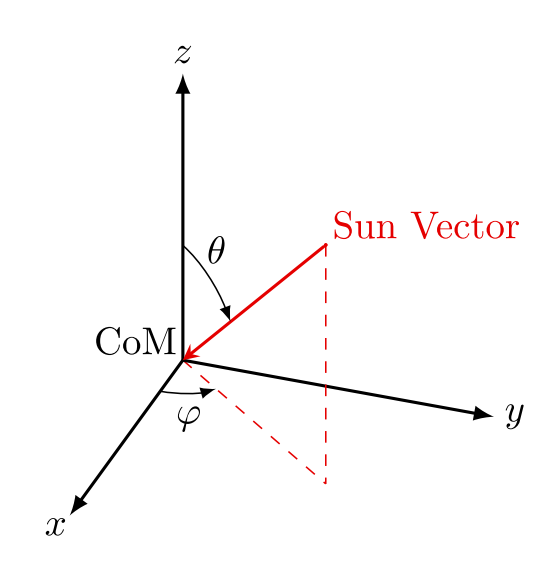
This section presents the retrieved gravity field models from ll-SST type of missions with the different satellite shapes, diverse performance of the SGRS optical accelerometers and various air drag coefficients, respectively.

Figure 9 shows a degree root mean square (RMS) of the spherical harmonic coefficient differences between recovered and reference gravity fields (true errors) for the case of the 'standard' GRACE-FO trapezoidal prism shape (blue curve) and of two modified shapes (orange and green curves) with a single solar panel that is mounted either on bottom or top of satellite body. Note that in the 'standard' GRACE-FO case a simulated SGRS optical accelerometer with LRI 2033 was also considered. Using identical inertial and inter-









(b) Satellite center of mass (CoM), satellite reference coordinate system and incident sun vector.

Fig. 5 Precalculated SRP force for orbital simulation

satellite range sensors enables a fair comparison of different scenarios, highlighting performance variations due to satellite shape differences. In the corresponding orbit simulations, a drag coefficient $c_D = 2.25$ was taken for the standard shape and $c_D = 3.0$ for the modified ones in order to incorporate the increased surface area from the solar panels (sect. 3.1). Relevant cross-sectional areas of the satellite were also considered in deriving the SGRS noise time series, as its actuation noise depends on the effective area (sect. 3.2) and depicted in Fig. 4. Also, the gray dashed-dotted line represents the mean monthly time-variable signal from the terrestrial hydrosphere (H), continental ice sheets and mountain glaciers (I) as well as solid Earth deformations (S), or shortly HIS (Dobslaw et al. 2015). Although time-variable background models and their associated errors are among the dominant error sources in current satellite gravimetry missions, they were not included in this GFR study. Since the focus here is on evaluating how modifications to GRACE-like satellites impact gravity field recovery, particularly in relation to the changing performance of inertial sensors (accelerometers) with different satellite shapes. The gray dash-dotted curve is presented to illustrate that, in an idealized scenario where temporal aliasing is sufficiently accounted for and high-performance instruments are fully utilized, a time-variable gravity field could potentially be determined up to approximately degree 60 in both modified cases.

Figure 9 also shows that the more complex satellite shapes with a single solar panel, mounted either on top or bottom

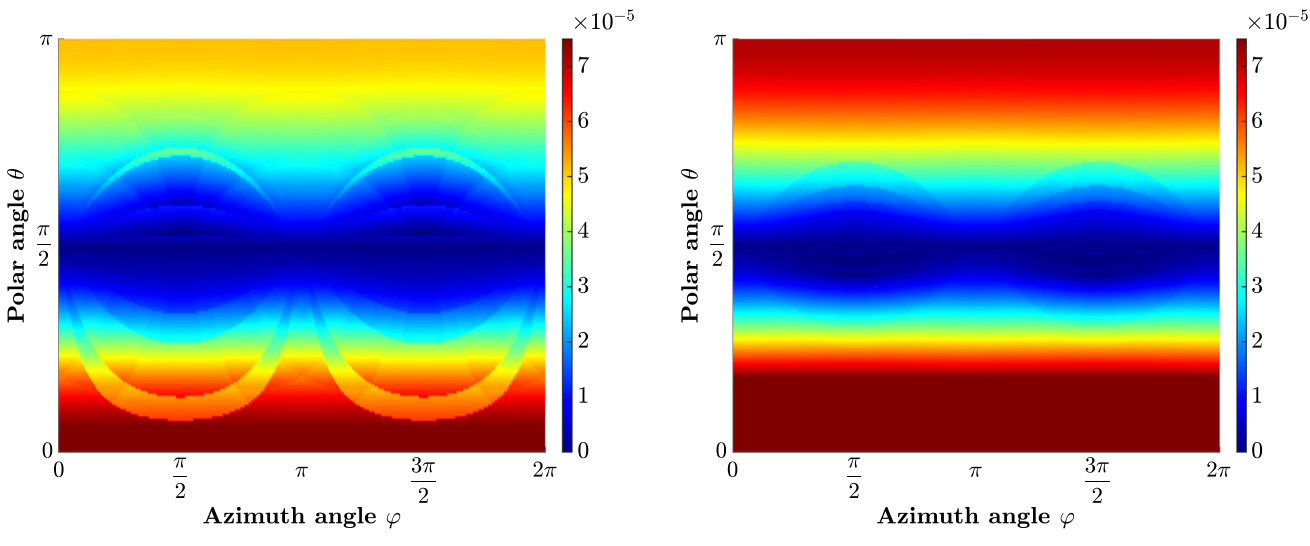
of the satellite body, do not significantly reduce the quality of the science output. The difference between the modified cases and the standard one, comes, in our optimistic study with multiple simplifications and assumptions that lead to several error sources and uncertainties listed in the Table 4, mainly from the different level of the actuation the noise of SGRS w.r.t. cross-sectorial area that was explained in sect. 3.2. The convergence of the orange and green curves for the modified cases can be explained by their similar rates of orbital decay (see Fig. 7b) and the consistent performance levels of the modeled SGRS (see Fig. 4).

Figure 10 shows the degree RMS of the spherical harmonic coefficient differences, plotted in geoid height, for the 'standard' GRACE-FO and two modified cases with double solar arrays (cross-sectorial area 1.47 m²) w.r.t. mean monthly HIS signal. Residuals in the spectral domain from the alternative designs are slightly larger than from the standard case. Similar to the previous simulation with a single solar panel, here this difference is mainly due to the different level of the actuation noise of the SGRS (see Fig. 4). Again, here both advanced scenarios converged due the identical rate of the orbit decay (see Fig. 7b).

Both figs. 9 and 10 show that GRACE-like satellites with single or double solar arrays provide slightly lower accuracy in retrieved gravity models compared to the GRACE-FO standard shape. It is important to note that these GFR results reflect the combined influence of orbital dynamics and SGRS performance, both affected by satellite shape. If the opti-

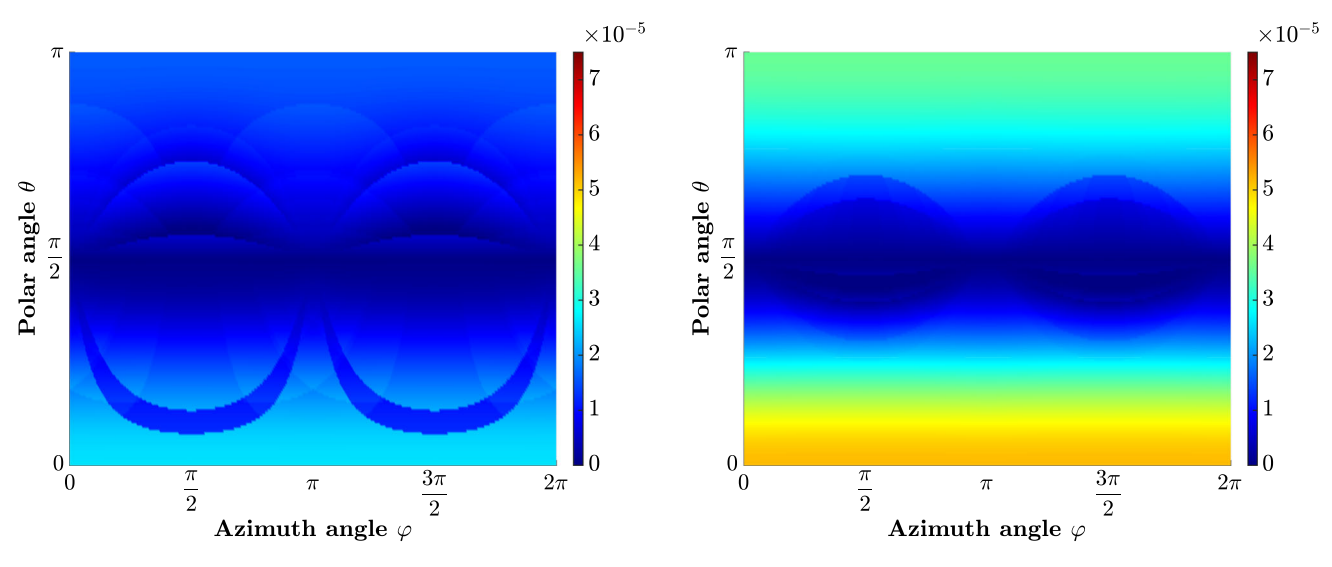


59 Page 14 of 19 A. Leipner et al.



(a) GRACE-like shape (double solar panel top)

(b) GRACE-like shape (double solar panel bottom)



(c) GRACE-like shape (single solar panel top)

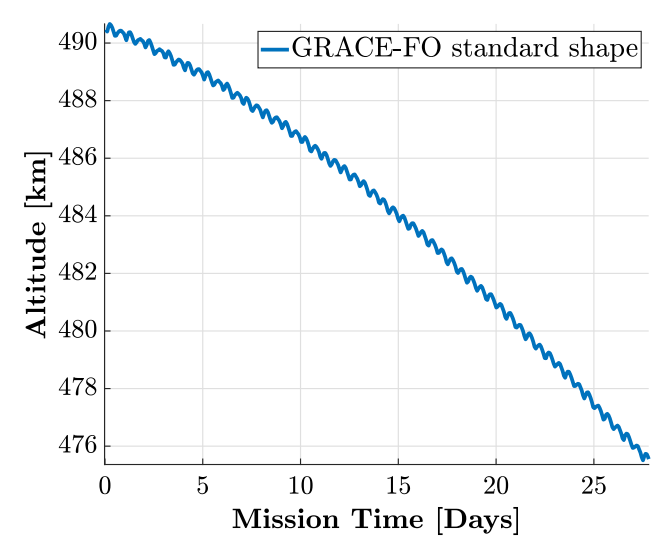
(d) GRACE-like shape (single solar panel bottom)

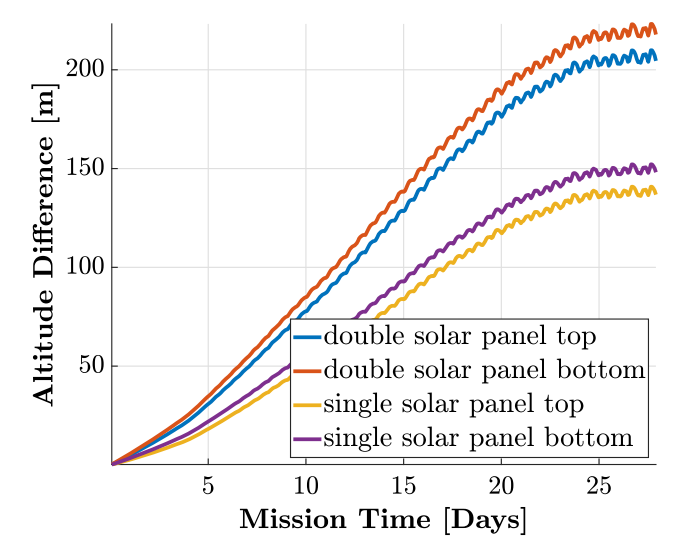
Fig. 6 SRP force difference in newton of the studied satellite shapes to the standard GRACE-FO shape

cal accelerometer performance were independent of satellite shape, modified satellites-experiencing faster orbit decay (Fig. 7b)-would achieve higher gravity field recovery accuracy. However, our carried out GFR simulations indicate that the SGRS performance deteriorates in the mid-frequency domain for modified satellite designs (Fig. 4), outweighing the benefits of stronger orbit decay. In summary, the reduced SGRS performance on modified satellites leads to less accurate GFR solutions, despite their lower orbits compared to the GRACE-FO standard shape.

In order to verify whether the observed difference of residuals in the spectral domain between the standard and modified cases with single and double solar arrays, depicted in figs. 9 and 10, indeed occur mostly due to the different SGRS performance above 1 mHz, additional orbit and GFR simulations have been carried out. Here only a GRACE-like satellite with a double panel mounted on bottom was considered, but with two other air drag coefficients $c_D=2.65$ and $c_D=4.5$ (representing the critical case, i.e., doubled value of the drag coefficient for the standard GRACE-FO shape). The same level of accuracy for the inertial sensor and LRI







- (a) Simulated decay of the maximum altitude per orbit of the GRACE-FO standard shape case (km).
- (b) Difference of the orbit decay of the modified cases ($C_D = 3.0$) w.r.t. GRACE-FO standard case (m).

Fig. 7 Absolute altitude of the standard GRACE-FO satellite over a one-month period and differences in altitude for various modified GRACE-like cases relative to the standard configuration

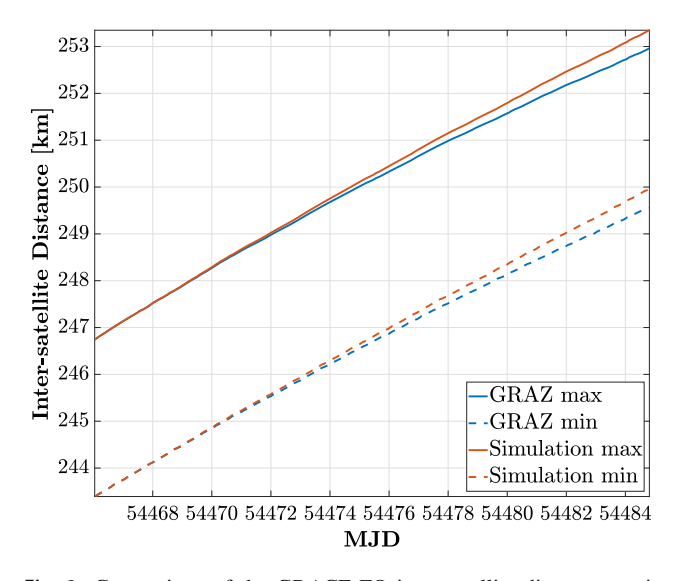


Fig. 8 Comparison of the GRACE-FO inter-satellite distance maximum and minimum values obtained from TU Graz (Mayer-Gürr et al. 2021) and simulated in XHPS within this study

was considered here. Degree RMS of the spherical harmonic coefficient differences for this GFR simulation are shown in Fig. 11. The GFR of this simulation shows that in spite of different orbit decays due to various drag coefficients, the order of magnitude of the Degree RMS curves in all three cases are the same. Therefore, it can be preliminary concluded that in the non-drag-compensated regime, when the orbit decay differs only by a few hundred meters w.r.t. the standard shape

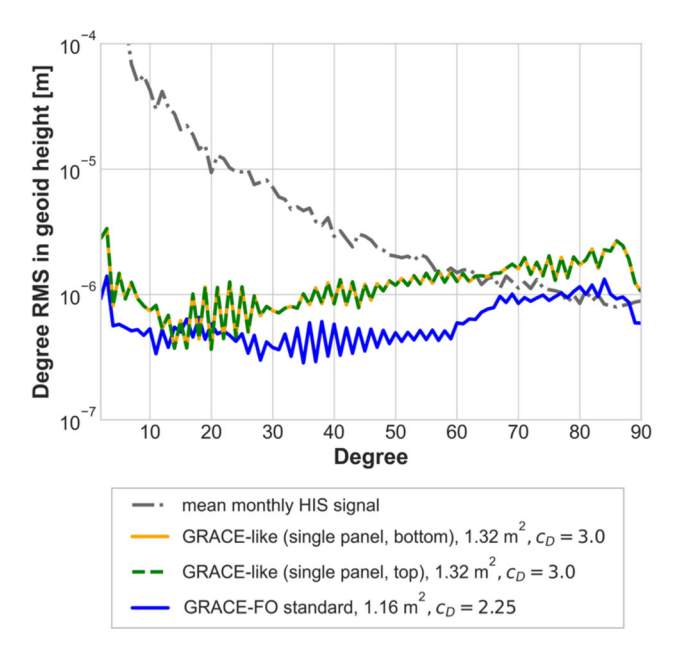


Fig. 9 Degree RMS of the spherical harmonic coefficient differences (true errors) between recovered and EIGEN-6C4 gravity field models in geoid height (m) using the GRACE-FO standard shape (blue curve) and two modified cases with single solar arrays (orange and green lines)

scenario (see Fig. 7b), the changing performance of the modeled SGRS w.r.t. the satellite shapes becomes the dominant factor affecting on GFR results.



59 Page 16 of 19
A. Leipner et al.

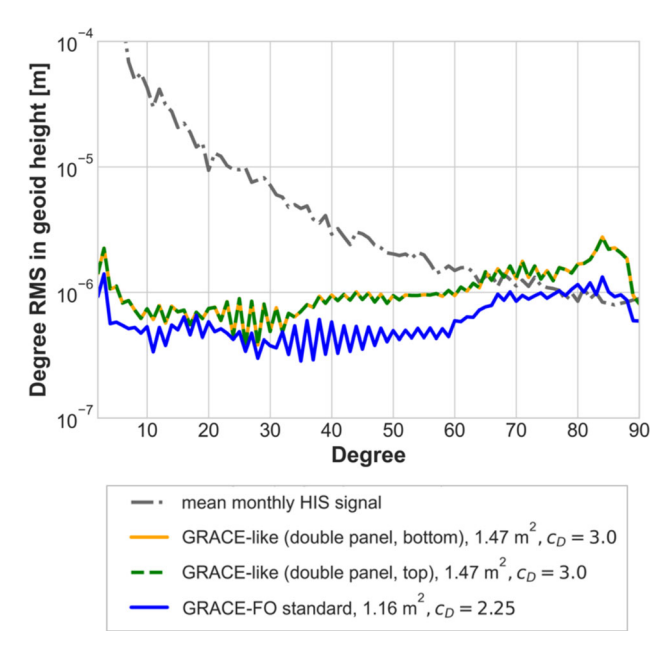


Fig. 10 Degree RMS of the spherical harmonic coefficient differences (true errors) between recovered and EIGEN-6C4 gravity field models in geoid height (m) from GRACE-FO standard shape (blue curve) and two modified cases with double solar arrays (orange and green lines)

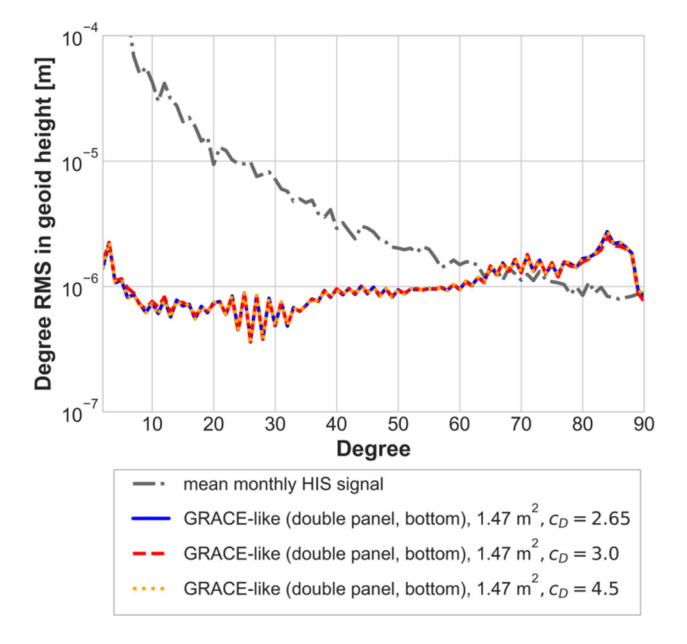


Fig. 11 Degree RMS of the spherical harmonic coefficient differences (true errors) between recovered and EIGEN-6C4 gravity field models in geoid height (m) from the GRACE-like shape with a double solar panel and three different drag coefficients

5 Discussion and conclusions

Future gravimetry missions may require increased power consumption due to drag-compensated regimes, advanced inertial sensors, and non-sun-synchronous orbital configurations. To meet these demands, a larger solar panel area is necessary. Additionally, the mass and volume constraints imposed by launch vehicle limitations make deployable solar panels a practical solution.

In this study closed-loop simulations including detailed orbit dynamics calculations, inertial sensor modeling, and gravity field recovery to evaluate the performance of future ll-SST gravimetry satellites with four modified shapes have been conducted. Finite element models were developed for the GRACE-FO trapezoidal prism and four GRACE-like satellites, each featuring either single or double solar panels mounted on the top or bottom of the satellite. These models were utilized in orbital simulations performed with XHPS, under the assumption that the satellite body was completely rigid. Therefore, no vibrations that might negatively impact the SGRS performance caused by the structural flexibility of the solar arrays were considered and evaluated. The SGRS, equipped with a laser interferometer TM readout, was modeled in ACME, accounting for performance variations due to coupling effects influenced by satellite shape. Finally, GFR simulations incorporated accelerometer noise time series, errors in the inter-satellite link, and various orbital scenarios generated in XHPS.

It is worth noting that eliminating of vibration effects was not the only simplification considered. In the XHPS satellite dynamics simulator, multiple numerical assumptions were incorporated into the simulations. These include approximations in the modeling of drag, SRP, orbit propagation, and numerical integration, as well as the exclusion of propellant consumption and orbital maneuvering effects. Similarly, in the GFR software QACC, the centrifugal term in the functional model was omitted, along with the effects of timevariable background models. Additionally, in the modeling of the SGRS noise budget within ACME, further assumptions were made, such as treating the system as a single degree of freedom and considering only air drag as non-gravitational perturbation.

Nevertheless, this simplified study provides a good preliminary assessment of the impact of different satellite shapes in a GRACE-like low-low satellite-to-satellite tracking (Il-SST) configuration on gravity field recovery. The results show that the residuals between the recovered and reference gravity field models obtained for the five satellite shapes are of a similar order of magnitude. However, as demonstrated in the orbital simulations, satellites equipped with extended solar panels exhibit a faster orbit decay compared to the standard GRACE-FO design. Specifically, the double-panel configurations showed an additional orbit decay of approxi-



mately 200 m per month relative to the standard GRACE-FO configuration, while the single-panel configurations exhibited a supplementary decay of about 150 m per month. These values would increase significantly under conditions of high solar activity or less accurate satellite attitude control systems.

Moreover, the increased surface area associated with extended solar panels leads to larger disturbance torques acting on the satellite, resulting in greater activity of the attitude control system to maintain attitude stability. In GRACE-like missions, which rely on magnetic torquers and cold gas thrusters for attitude and orbit control, this can result in more frequent thruster activations. Additionally, the larger surface area increases atmospheric drag, necessitating further thruster usage to maintain orbital altitude. Both effects contribute to higher overall fuel consumption.

Future improvements in the measurement of non-conservative forces are crucial for enhancing GFR performance in satellite gravimetry missions, particularly in scenarios involving larger disturbance torques caused by extended solar arrays. While this study employs an optical accelerometer (SGRS) due to its demonstrated advantages and proven flight heritage, additional performance gains could be realized by operating such sensors in a dragcompensated regime. As shown by Dávila Álvarez et al. (2022), the SGRS achieves higher accuracy under dragfree conditions due to the elimination of actuation noise. Therefore, integrating optical accelerometers with drag compensation systems thus represents a promising direction for future mission concepts, offering the dual benefit of mitigating non-conservative disturbances and improving instrument sensitivity.

An essential consideration emerging from this study is the trade-off presented by the modified satellite shapes: while the extended panels may support higher power requirements for future instruments, they also introduce challenges related to mission lifetime and the accuracy of the retrieved gravity models. This trade-off underscores the importance of a holistic approach to satellite design that balances these competing demands.

Another critical aspect that has to be taken into account, when utilizing the extended solar panels, is the field of view of the star cameras. They are located on the skewed sides of the satellite body and might be obscured by the extra solar panels. Therefore, certain workarounds are needed to maintain the necessary level of accuracy from the star cameras. One possible solution could be incorporating holes in the solar panels, when considering top-mounted solar panels.

Further studies should focus on addressing the limitations and simplifying assumptions made in this investigation to provide a more comprehensive understanding of the implications of modified satellite shapes on gravity field recovery performance. In principle, each of the considered software tools could be improved by considering additional parameters or enhanced models and routines. Incorporating time-variable background models and associated aliasing effects would allow for a more realistic simulation of operational conditions. Additionally, refining the modeling of non-gravitational forces by including satellite vibrations and propellant consumption would improve the accuracy of the satellite dynamics simulations. Enhanced thermal noise modeling and a broader exploration of different inertial sensor configurations, including advanced hybrid or quantum-based sensors, could also be pursued. Finally, the analysis should be extended to include variations in orbit scenarios, such as high solar activity periods and alternative orbital inclinations, to better evaluate the trade-offs between mission duration, attitude stability, and gravity field recovery accuracy.

Funding Open Access funding enabled and organized by Projekt DEAL.

Data availability The datasets generated during and/or analyzed during the current study are available from the corresponding author on reasonable request.

Declarations

Funding The authors acknowledge funding by Deutsche Forschungsgemeinschaft (DFG) - TerraQ (Project-ID 434617780 - SFB 1464).

Conflict of interest The authors declare that they have no known competing financial interests or personal relationships that could have appeared to influence the work reported in this paper.

Author Contributions A. Le., A. Ku., A. Re., A. Kn., M. Sc. and M. Li. contributed to conceptualization; A. Le., A. Ku., A. Re. and M. We. provided methodology; A. Le., A. Ku. and A. Re. performed formal analysis, simulation and investigation; A. Le., A. Ku. and A. Re. performed writing-original draft preparation; A. Le., A. Ku., A. Re., A. Kn., M. Sc., M. Li., V. Mü., M. We., J. Mü. performed writing-review and editing.

Open Access This article is licensed under a Creative Commons Attribution 4.0 International License, which permits use, sharing, adaptation, distribution and reproduction in any medium or format, as long as you give appropriate credit to the original author(s) and the source, provide a link to the Creative Commons licence, and indicate if changes were made. The images or other third party material in this article are included in the article's Creative Commons licence, unless indicated otherwise in a credit line to the material. If material is not included in the article's Creative Commons licence and your intended use is not permitted by statutory regulation or exceeds the permitted use, you will need to obtain permission directly from the copyright holder. To view a copy of this licence, visit http://creativecommons.org/licenses/by/4.0/.

References

Armano M, Audley H, Baird J, et al (2021) Sensor Noise in LISA Pathfinder: In-Flight Performance of the Optical Test Mass Read-



- out. Physical Review Letters 126(13). https://doi.org/10.1103/PhysRevLett.126.131103
- Brockmann JM, Zehentner N, Höck E et al (2014) EGM_TIM_RL05: An independent geoid with centimeter accuracy purely based on the GOCE mission. Geophysical Research Letters 41(22):8089– 8099
- van Camp M, dos Santos FP, Murböck M et al (2021) Lasers and ultracold atoms for a changing Earth. Eos, Transactions American Geophysical Union 102. https://doi.org/10.1029/2021EO210673
- Canuto E (2018) Spacecraft Dynamics and Control: The Embedded Model Control Approach. Aerospace Engineering Ser, Elsevier Science & Technology, Saint Louis, https://ebookcentral.proquest.com/lib/kxp/detail.action?docID=5320158
- Cappellari JO (ed) (1976) Mathematical theory of the Goddard trajectory determination system. Washington, DC, https://permalink. obvsg.at/AC00507166
- Chen J, Cazenave A, Dahle C et al (2022) Applications and challenges of GRACE and GRACE Follow-On satellite gravimetry. Surveys in Geophysics 43(1):305–345. https://doi.org/10.1007/s10712-021-09685-x
- Christophe B, Foulon B, Liorzou F, et al (2018) Status of development of the future accelerometers for next generation gravity missions. In: International Symposium on Advancing Geodesy in a Changing World: Proceedings of the IAG Scientific Assembly, Kobe, Japan, July 30–August 4, 2017, Springer, pp 85–89, https://doi.org/10. 1007/1345_2018_42
- Dalin M, Lebat V, Boulanger D, et al (2020) ONERA accelerometers for future gravity mission. In: EGU General Assembly Conference Abstracts, p 5721, https://doi.org/10.5194/egusphere-egu2020-5721
- Daras I, March G, Pail R et al (2023) Mass-change And Geosciences International Constellation (MAGIC) expected impact on science and applications. Geophysical Journal International 236(3):1288– 1308. https://doi.org/10.1093/gji/ggad472
- Dávila Álvarez A, Knudtson A, Patel U et al (2022) A simplified gravitational reference sensor for satellite geodesy. Journal of Geodesy 96(10):70. https://doi.org/10.1007/s00190-022-01659-0
- Dionisio S, Anselmi A, Bonino L, et al (2018) The "Next Generation Gravity Mission": challenges and consolidation of the system concepts and technological innovations. In: 2018 SpaceOps Conference. American Institute of Aeronautics and Astronautics, Reston, Virginia, https://doi.org/10.2514/6.2018-2495
- Dobslaw H, Bergmann-Wolf I, Dill R et al (2015) The updated ESA Earth System Model for future gravity mission simulation studies. Journal of Geodesy 89:505–513. https://doi.org/10.1007/s00190-014-0787-8
- Flechtner F, Reigber C, Rummel R et al (2021) Satellite gravimetry: a review of its realization. Surveys in Geophysics 42(5):1029–1074. https://doi.org/10.1007/s10712-021-09658-0
- Folkner WM, Williams JG, Boggs DH et al (2014) The Planetary and Lunar Ephemerides DE430 and DE431. Interplanetary Network Progress Report 42–196:1–81
- Förste C, Bruinsma S, Abrikosov O, et al (2014) Eigen-6c4 the latest combined global gravity field model including goce data up to degree and order 2190 of gfz potsdam and grgs toulouse. https://doi.org/10.5880/icgem.2015.1
- Haagmans R, Siemes C, Massotti L et al (2020) ESA's next-generation gravity mission concepts. Rendiconti Lincei Scienze Fisiche e Naturali 31(S1):15–25. https://doi.org/10.1007/s12210-020-00875-0
- Halloin H, Prat P, Brossard J (2013) Long term characterization of voltage references. arXiv preprint arXiv:1312.5101 https://doi.org/10.48550/arXiv.1312.5101
- Hassa CL (2013) Drag coefficient estimation using satellite attitude and orbit data. Master's thesis, The Pennsylvania State University, https://etda.libraries.psu.edu/catalog/19949, master of Science thesis

- Heller-Kaikov B, Pail R, Daras I (2023) Mission design aspects for the mass change and geoscience international constellation (MAGIC). Geophysical Journal International 235(1):718–735
- HosseiniArani A, Schilling M, Beaufils Q et al (2024) Advances in atom interferometry and their impacts on the performance of quantum accelerometers on-board future satellite gravity missions. Advances in Space Research. https://doi.org/10.1016/j.asr.2024. 06.055
- Humphrey V, Rodell M, Eicker A (2023) Using satellite-based terrestrial water storage data: a review. Surveys in Geophysics 44(5):1489–1517. https://doi.org/10.1007/s10712-022-09754-9
- Josselin V, Touboul P, Kielbasa R (1999) Capacitive detection scheme for space accelerometers applications. Sensors and Actuators A: Physical 78(2–3):92–98. https://doi.org/10.1016/S0924-4247(99)00227-7
- Kang K, Zhong S, Geruo A et al (2022) The effects of non-newtonian rheology in the upper mantle on relative sea level change and geodetic observables induced by glacial isostatic adjustment process. Geophysical Journal International 228(3):1887–1906. https://doi.org/10.1093/gji/ggab428
- Knabe A (2023) New concepts for gravity field recovery using satellites. PhD thesis, Wissenschaftliche Arbeiten der Fachrichtung Geodäsie und Geoinformatik der Leibniz Universität Hannover; ISSN 0174-1454, Nr. 391
- Koch K, Kuhlmann H, Schuh WD (2010) Approximating covariance matrices estimated in multivariate models by estimated auto-and cross-covariances. Journal of geodesy 84:383–397. https://doi.org/ 10.1007/s00190-010-0375-5
- Kornfeld RP, Arnold BW, Gross MA et al (2019) GRACE-FO: The Gravity Recovery and Climate Experiment Follow-On mission. Journal of Spacecraft and Rockets 56(3):931–951. https://doi.org/ 10.2514/1.A34326
- Kupriyanov A, Reis A, Knabe A et al (2024a) Analysis of novel sensors and satellite formation flights for future gravimetry missions. International Association of Geodesy Symposia. https://doi.org/ 10.1007/1345_2024_279
- Kupriyanov A, Reis A, Schilling M et al (2024b) Benefit of enhanced electrostatic and optical accelerometry for future gravimetry missions. Advances in Space Research 73. https://doi.org/10.1016/j. asr.2023.12.067
- Kupriyanov A (2025) Investigation of optical accelerometry and novel satellite formations for future gravimetry missions. Wissenschaftliche Arbeiten der Fachrichtung Geodäsie und Geoinformatik der Leibniz Universität Hannover. https://doi.org/10.15488/ 19007
- List M, Bremer S, Rievers B et al (2015) Modelling of solar radiation pressure effects: Parameter analysis for the MICROSCOPE mission. International Journal of Aerospace Engineering 2015:1–14. https://doi.org/10.1155/2015/928206
- LUIS (2024) Lena Compute Cluster. Projektnummer for Lena compute cluster is INST 187/592-1 FUGG. Leibniz University IT Services
- Luthcke SB, Sabaka T, Loomis B et al (2013) Antarctica, Greenland and Gulf of Alaska land-ice evolution from an iterated GRACE global mascon solution. Journal of Glaciology 59(216):613–631. https://doi.org/10.3189/2013JoG12J147
- Mance D (2012) Development of electronic system for sensing and actuation of test mass of the inertial sensor LISA. PhD thesis, Faculty of Electrical Engineering, Mechanical Engineering and Naval Architecture, University of Split
- Mayer-Gürr T, Behzadpour S, Eicker A et al (2021) Groops: A software toolkit for gravity field recovery and gnss processing. Computers & Geosciences 155:104864. https://doi.org/10.1016/j.cageo. 2021.104864
- Moe K, Moe MM (2005) Gas-surface interactions and satellite drag coefficients. Planetary and Space Science 53(8):793–801. https:// doi.org/10.1016/j.pss.2005.03.005



- Montenbruck O, Gill E, Lutze F (2002) Satellite orbits: models, methods, and applications. Appl Mech Rev 55(2):B27–B28. https://doi.org/10.1115/1.1451162
- Müller V, Hauk M, Misfeldt M et al (2022) Comparing GRACE-FO KBR and LRI ranging data with focus on carrier frequency variations. Remote Sensing 14(17):4335. https://doi.org/10.3390/rs14174335
- NASA (2002) GRACE Launch. Press Kit, National Aeronautics and Space Administration, Washington, DC
- Niemeier W (2008) Ausgleichungsrechnung: Statistische Auswertemethoden, 2nd edn. de Gruyter Lehrbuch, De Gruyter, Berlin
- Otosaka IN, Shepherd A, Ivins ER et al (2022) Mass balance of the greenland and antarctic ice sheets from 1992 to 2020. Earth System Science Data Discussions 2022:1–33. https://doi.org/10.5194/essd-15-1597-2023
- Pail R, Bingham R, Braitenberg C et al (2015) Science and user needs for observing global mass transport to understand global change and to benefit society. Surveys in Geophysics 36(6):743–772. https://doi.org/10.1007/s10712-015-9348-9
- Pail R, Bamber J, Biancale R et al (2019) Mass variation observing system by high low inter-satellite links (MOBILE)-a new concept for sustained observation of mass transport from space. Journal of Geodetic Science 9(1):48–58. https://doi.org/10.1515/jogs-2019-0006
- Peidou A, Landerer F, Wiese D, et al (2022) Spatiotemporal characterization of geophysical signal detection capabilities of GRACE–FO. Geophysical Research Letters 49(1). https://doi.org/10.1029/2021GL095157
- Pfaffenzeller N, Pail R (2023) Small satellite formations and constellations for observing sub-daily mass changes in the earth system. Geophysical Journal International 234(3):1550–1567
- Picone JM, Hedin AE, Drob DP, et al (2002) NRLMSISE–00 empirical model of the atmosphere: Statistical comparisons and scientific issues. Journal of Geophysical Research: Space Physics 107(A12). doi:https://doi.org/10.1029/2002JA009430
- Purkhauser AF, Pail R (2020) Triple-pair constellation configurations for temporal gravity field retrieval. Remote Sensing 12(5):831
- Rievers B, Bremer S, List M, et al (2019) Evaluating atmospheric density with MICROSCOPE data. Paper presented at the 70th International Astronautical Congress (IAC), Washington D.C
- Satsearch (2024) Solar cell array 30% triple junction gaas. https://satsearch.co/products/oce-technology-solar-cell-array-triple-junction-gaas?__cf_chl_tk=Kt8K.
 tJ8ITgitfyk3yPzt4KpOJswLPaadpe4DNd8taY-17265649140.0.1.1-5140
- Shihora L, Balidakis K, Dill R, et al (2022) Non-tidal background modeling for satellite gravimetry based on operational ECWMF and ERA5 reanalysis data: AOD1B RL07. Journal of Geophysical Research: Solid Earth 127(8). https://doi.org/10.1029/ 2022JB024360
- Shihora L, Liu Z, Balidakis K et al (2024) Accounting for residual errors in atmosphere-ocean background models applied in satellite gravimetry. Journal of Geodesy 98(4):27. https://doi.org/10.1007/s00190-024-01832-7
- Sun AY, Scanlon BR, AghaKouchak A et al (2017) Using GRACE satellite gravimetry for assessing large-scale hydrologic extremes. Remote Sensing 9(12):1287. https://doi.org/10.3390/rs9121287

- Tapley BD, Watkins MM, Flechtner F et al (2019) Contributions of GRACE to understanding climate change. Nature Climate Change 5(5):358–369. https://doi.org/10.1038/s41558-019-0456-2
- Torge W, Müller J, Pail R (2023) Geodesy, 5th edn. De Gruyter Textbook, De Gruyter, Berlin and Boston, https://doi.org/10.1515/9783110723304
- Weber WJ, Bortoluzzi D, Bosetti P et al (2022) Application of LISA gravitational reference sensor hardware to future intersatellite geodesy missions. Remote Sensing 14(13):3092. https://doi.org/ 10.3390/rs14133092
- Weigelt M (2017) The acceleration approach. In: Naeimi M, Flury J (eds) Global Gravity Field Modeling from Satellite-to-Satellite Tracking Data. Lecture Notes in Earth System Sciences, Springer International Publishing, Cham, p 97–126, https://doi.org/10.1007/978-3-319-49941-3_4
- Wen HY, Kruizinga G, Paik M, et al (2019) Gravity Recovery and Climate Experiment Follow-On (GRACE-FO) Level-1 Data Product User Handbook, JPL Publication D-56935. ftp://podaac-ftp.jpl.nasa.gov/allData/gracefo/docs/GRACE-FO_L1_Handbook_JPL-D-56935_20190521.pdf
- Wertz JR (ed) (1980) Spacecraft attitude determination and control, Astrophysics and space science library, vol 73. Reidel, Dordrecht
- Wiese DN, Bienstock B, Blackwood C et al (2022) The mass change designated observable study: overview and results. Earth and Space Science 9(8):e2022EA002311. https://doi.org/10.1029/2022EA002311
- Wöske F, Kato T, List M, et al (2016) Development of a high precision simulation tool for gravity recovery missions like GRACE. In: Zanetti R, Russel R, Ozimek M, et al (eds) Proceedings of the 26th AAS/AIAA space flight mechanics meeting held February, pp 2445–2457
- Wöske F, Kato T, Rievers B et al (2018) GRACE accelerometer calibration by high precision non-gravitational force modeling. Advances in Space Research 63(3):1318–1335. https://doi.org/10.1016/j.asr. 2018.10.025
- Wu H (2016) Gravity field recovery from GOCE observations. PhD thesis, Wissenschaftliche Arbeiten der Fachrichtung Geodäsie und Geoinformatik der Leibniz Universität Hannover; ISSN 0174-1454, Nr. 324
- Zahzam N, Christophe B, Lebat V et al (2022) Hybrid electrostaticatomic accelerometer for future space gravity missions. Remote Sensing 14(14):3273. https://doi.org/10.3390/rs14143273
- Zotov L, Bizouard C, Shum C et al (2022) Analysis of earth's polar motion and length of day trends in comparison with estimates using second degree stokes coefficients from satellite gravimetry. Advances in Space Research 69(1):308–318. https://doi.org/10.1016/j.asr.2021.09.010

